MODELING VARIABLE-DENSITY GROUNDWATER FLOW AND SOLUTE TRANSPORT IN COMPLEX FRACTURE NETWORKS

Thomas Graf, Département de géologie et génie géologique, Université Laval, Québec, Canada
René Therrien, Département de géologie et génie géologique, Université Laval, Québec, Canada

ABSTRACT
The numerical model HydroSphere has been modified to account for variable-density flow and solute transport in porous fractured media. A general formulation of the body force vector is derived such that density effects can be simulated in fractures of any arbitrary inclination. Irregular fracture networks can also be randomly generated by HydroSphere. Thus, the new model allows investigating dense plume migration in more disorganized fractured media than done previously. A series of scenarios in various, yet statistically equivalent, fracture networks were conducted and solute migration proved to be highly sensitive to the network. A sensitivity analysis revealed that low fracture apertures, low matrix permeability, high matrix porosity and large molecular diffusion tend to stabilize solute migration.

RÉSUMÉ
Le modèle numérique HydroSphere a été modifié pour simuler l'écoulement et le transport à densité variable dans des milieux fracturés. Une formulation générale du vecteur de flottabilité a été dérivée de sorte que des effets de densité peuvent être simulés dans des fractures à inclinaison arbitraire. Des réseaux irréguliers de fractures peuvent aussi être générés par HydroSphere. Ainsi, le nouveau modèle permet d'étudier la migration de soluté dans un milieu irrégulièrement fracturé. Une série de simulations pour différents réseaux de fractures statistiquement équivalents indique que le transport de masse avec effet de densité est fortement influencé par le réseau de fractures. Une analyse de sensibilité a démontré que la diminution de l'ouverture des fractures et de la conductivité du milieu poreux, ainsi que l'augmentation de la porosité et du coefficient de diffusion moléculaire tendent à stabiliser le système.

1. INTRODUCTION

In subsurface environments, noxious contaminants are mainly transported by the groundwater. Spatiotemporal variations of the groundwater density greatly affect the transport pattern of solutes in various geological media. Examples for density-driven flow and transport can be found in many areas of subsurface hydrology, oceanography, meteorology, geophysics and nuclear waste management.

Nuclear waste management underlines the importance of studying variable-density flow and transport. The safe disposal of nuclear waste is commonly regarded as feasible in low-permeability geological media at a depth of up to 1000 m (AECL, 1994). At such depths, the groundwater is a dense Ca-Na-Cl brine. Acute safety questions regarding nuclear waste repository arise due to the presence of fractures in the rock formations.

Fractures greatly impact mass transport, because they represent preferential pathways where accidentally released radionuclides migrate at velocities that are several orders of magnitude larger than within the rock matrix. Clearly, it is of paramount importance to understand the movement of contaminants in fractured media under the influence of variable water density.

Variable-density transport has been intensely studied in diverse subsurface environments, predominantly in homogeneous and heterogeneous porous media (Figure 1a and 1b).

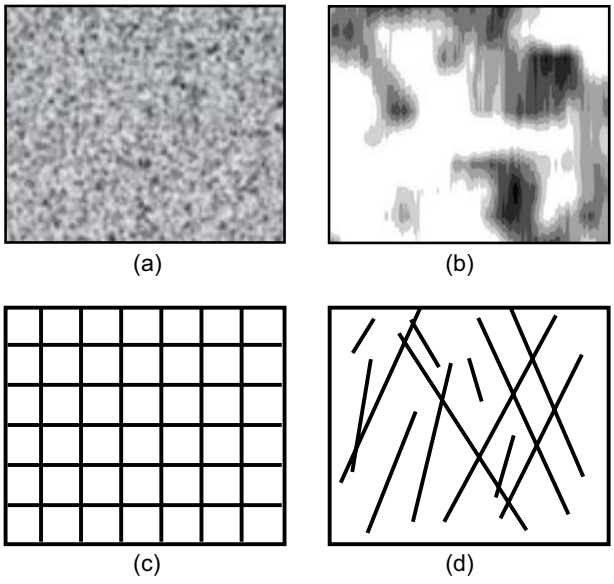

Figure 1. Different styles of geological media: (a) homogeneous porous medium, (b) heterogeneous porous medium, (c) fractured medium consisting of vertical and horizontal fractures and (d) fractured geological medium with nonuniform fracture aperture, trace and orientation (modified from Simmons et al., 2001).

Shikaze et al. (1998) investigated the migration of dense plumes in discretely-fractured media, using an orthogonal fracture network embedded in a porous matrix (Figure 1c). They found that dense solute plumes may develop in a

highly irregular fashion and the uncertainty associated with prediction can be very high.
However, Shikaze et al.'s (1998) research was limited to a regular fracture distribution and uniform fracture apertures. Therefore, how dense plume instabilities will develop in fractured networks with an irregular pattern (Figure 1d) remains unknown.
To address this question, the HydroSphere model (Therrien and Sudicky, 1996), which solves 3D variably-saturated flow and solute transport in discretely-fractured porous media, has been modified to account for density variations in irregular fracture networks.

2. NUMERICAL MODEL

In HydroSphere, the discrete fracture approach is used for flow and transport in fractured porous media, and two-dimensional fracture elements and three-dimensional matrix elements share common nodes in the 3D grid. Governing equations for flow and transport have to be formulated such that the common nodes receive contributions from the porous matrix as well as from the fractures.

2.1 Flow and Transport Variables

The flow variable used in HydroSphere is the equivalent freshwater head h_0 [L], defined in Frind (1982) as

$$h_0 = \frac{P}{\rho_0 g} + z \qquad [1]$$

where P [M L^{-1} T^{-2}] is the dynamic fluid pressure, ρ_0 [M L^{-3}] is the freshwater density, g [L T^{-2}] is the gravitational acceleration and z [L] is the elevation above datum.
The transport variable used in HydroSphere is the dimensionless relative concentration c, which varies between 0 and 1. It is linked with density through the linear relationship

$$\rho_r = \gamma c \qquad [2]$$

where ρ_r is the dimensionless relative density, defined in Frind (1982) as

$$\rho_r = \frac{\rho}{\rho_0} - 1 \qquad [3]$$

where ρ [M L^{-3}] is the fluid density. The dimensionless constant γ is the maximum relative density given by

$$\gamma = \frac{\rho_{max}}{\rho_0} - 1 \qquad [4]$$

where the assumption is made that the solute concentration for a fluid of density $\rho=\rho_{max}$ is $c_{max}=1$.

2.2 Governing Equations in Porous Media

With the equivalent freshwater head, the Darcy flux q_i [L T^{-1}] can be completely expressed in terms of freshwater properties:

$$q_i = -K_{ij}^0 \left(\frac{\partial h_0}{\partial x_j} + \gamma c \eta_j \right) \qquad i,j = 1,2,3 \qquad [5]$$

where K_{ij}^0 [L T^{-1}] is the freshwater hydraulic conductivity tensor and η_j is a dimensionless indicator for the flow direction. A value of η_j=1 indicates the vertical direction while η_j=0 indicates both horizontal directions (Frind, 1982). Note that, compared to the standard Darcy equation, the additional body force term $\gamma c \eta_j$ accounts for spatial fluid density variations.
The three-dimensional governing equation for variable-density flow in porous media under saturated conditions is (Frind, 1982):

$$\frac{\partial}{\partial x_i} \left[K_{ij}^0 \left(\frac{\partial h_0}{\partial x_j} + \gamma c \eta_j \right) \right] = S_S \frac{\partial h_0}{\partial t} \qquad i,j = 1,2,3 \qquad [6]$$

The specific storage S_S [L^{-1}] accounts for both matrix and fluid compressibility. It is defined as

$$S_S = \rho_0 g (\alpha_m + \phi \alpha_{fl}) \qquad [7]$$

and does not vary with fluid density. Matrix porosity is given by ϕ [--] and α_m [M^{-1} L T^2] and α_{fl} [M^{-1} L T^2] are the matrix and fluid compressibility, respectively.
Neglecting adsorption, radioactive decay and solute sources/sinks, the three-dimensional advective-dispersive equation governing solute transport is given by

$$\frac{\partial}{\partial x_i} \left(\phi D_{ij} \frac{\partial c}{\partial x_j} - q_i c \right) = \frac{\partial (\phi c)}{\partial t} \qquad i,j = 1,2,3 \qquad [8]$$

which is identical to the transport equation for the usual case of constant fluid density. The coefficients of the hydrodynamic dispersion tensor D_{ij} [L^2 T^{-1}] are given by Bear (1988) as

$$\phi D_{ij} = (\alpha_l - \alpha_t) \frac{q_i q_j}{|q|} + \alpha_t |q| \delta_{ij} + \phi \tau D_d \delta_{ij} \qquad i,j = 1,2,3 \qquad [9]$$

where α_l [L] and α_t [L] are the longitudinal and transverse dispersivity, respectively, δ_{ij} [--] is the Kronecker delta function, τ [--] the factor of matrix tortuosity and D_d [L^2 T^{-1}] the free-solution diffusion coefficient.

2.3 Governing Equations in Fracture Media

The Darcy flux in fractures is calculated similarly to the flux computation in porous media (Equation 5):

$$q_i^{fr} = -K_0^{fr}\left(\frac{\partial h_0^{fr}}{\partial x_j} + \gamma c^{fr}\eta_j\right) \qquad i,j=1,2 \qquad [10]$$

where superscript "fr" refers to the fracture media. The freshwater hydraulic conductivity of the fracture, K_0^{fr} [L T^{-1}], can be evaluated as

$$K_0^{fr} = \frac{(2b)^2 \rho_0 g}{12\mu} \qquad [11]$$

where 2b [L] is the fracture aperture and μ [M L^{-1} T^{-1}] is the dynamic viscosity of the fluid. However, as opposed to the Darcy equation in a porous matrix element (Equation 5), in a fracture element, the indicator for flow direction η_j is a function of the fracture slope φ, defined in Figure 2. According to Bear (1988, p. 169), the body force term in inclined fracture elements is weighted by the cosine of the fracture incline φ.

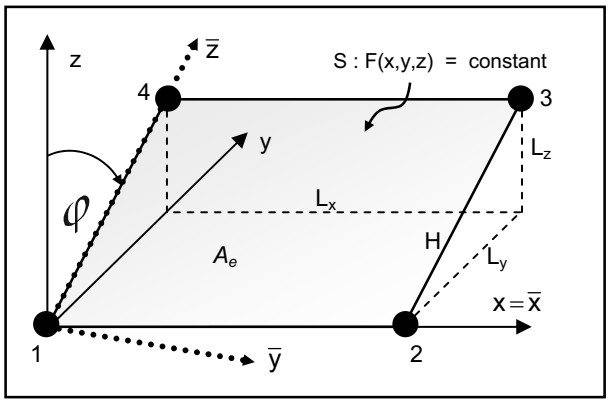

Figure 2. Geometry of an inclined fracture element (face) in three dimensions.

Thus, the Darcy equation for a fracture element of any arbitrary slope is given by

$$q_i^{fr} = -K_0^{fr}\left(\frac{\partial h_0^{fr}}{\partial x_j} + \gamma c^{fr}\cos\varphi\right) \qquad i,j=1,2 \qquad [12]$$

The variable-density flow equation in fractured media is given by Shikaze et al. (1998) for the case of only vertical and horizontal fractures. Using Equation 12, the governing flow equation can be written in the general form

$$(2b)\left\{\frac{\partial}{\partial x_i}\left[K_0^{fr}\left(\frac{\partial h_0^{fr}}{\partial x_j} + \gamma c^{fr}\cos\varphi\right)\right] - S_S^{fr}\frac{\partial h_0^{fr}}{\partial t}\right\} + q_{n|l^+} - q_{n|l^-} = 0$$

$$i,j=1,2 \qquad [13]$$

where the final two terms represent normal components of fluid flux across the boundary interfaces (l^+ and l^-) that separate the fracture and the porous matrix. The specific storage in the fracture, S_S^{fr} [L^{-1}], can easily be derived from Equation 7 by assuming that the fracture is incompressible, such that α_m=0, and by setting its porosity to 1:

$$S_S^{fr} = \rho_0 g \alpha_{fl} \qquad [14]$$

Shikaze et al. (1998) also provide the governing equation for variable-density transport in fractured media, which is not different from the case of constant fluid density.

$$(2b)\left[\frac{\partial}{\partial x_i}\left(D_{ij}^{fr}\frac{\partial c^{fr}}{\partial x_j} - q_i^{fr}c^{fr}\right) - \frac{\partial c^{fr}}{\partial t}\right] + \Omega_{n|l^+} - \Omega_{n|l^-} = 0$$

$$i,j=1,2 \qquad [15]$$

The final two terms represent advective-dispersive loss or gain of solute mass across the fracture-matrix interfaces l^+ and l^-. In Equation 15, D_{ij}^{fr} [L^2 T^{-1}] is the hydrodynamic dispersion coefficient of the fracture and can be calculated according to

$$D_{ij}^{fr} = \left(\alpha_l^{fr} - \alpha_t^{fr}\right)\frac{q_i^{fr}q_j^{fr}}{\left|q^{fr}\right|} + \alpha_t^{fr}\left|q^{fr}\right|\delta_{ij} + D_d\delta_{ij} \quad i,j=1,2 \qquad [16]$$

with α_l^{fr} [L] and α_t^{fr} [L] being the longitudinal and transverse fracture dispersivity, respectively.

2.4 Finite Element Formulation of the Flow Equation

HydroSphere uses the control volume finite element method (CVFE) to spatially discretize the flow equation. The basic principle of the finite element (FE) method is to, first, assume an approximate solution $\hat{h}_0$ for h_0 in the form

$$h_0 \approx \hat{h}_0 = \sum_{j=1}^{Nn} h_0^j w_j(x,y,z) \qquad [17]$$

where w_j are the elemental approximation functions and Nn is the total number of nodes in the finite element grid. The next step is to define a differential operator $L(h_0)$. The fractures and porous matrix share common nodes along the fracture walls and it is assumed that hydraulic head at the fracture/matrix interface, as well as concentration, are equal in both media. Therefore, the exchange terms $q_{n|l^+}$ and $q_{n|l^-}$ in Equation 13 vanish and $L(h_0)$ can be written as

$$L(h_0) = \frac{\partial}{\partial x_i}\left[K_0^{fr}\left(\frac{\partial h_0}{\partial x_j} + \gamma c\cos\varphi\right)\right] - S_S^{fr}\frac{\partial h_0}{\partial t} = 0 \qquad [18]$$

In Equation 18, the unknown exact solution h_0 is replaced by the approximation $\hat{h}_0$ such that the left hand side of Eq. 18 will be a nonzero residual. Hence, the third step is to weigh the residual by a weighting function ν_j and force the global integral of the weighted residual to zero:

$$\int_{\Omega} L(\hat{h}_0)\, \nu_i \, d\Omega = 0 \qquad \forall \nu_i \qquad [19]$$

where Ω is the model domain. In the common Galerkin method, weighting function ν_j is set equal the approximation function w_i. HydroSphere employs the CVFE method which ensures fluid mass conservation on both the elemental and the grid level. In the CVFE method, ν_j is chosen as 1, dividing the domain into subdomains or nodal control volumes. The finite element formulation of the balance equation (Equation 13) finally leads to a semi-discrete global matrix system in the compact form (Frind, 1982)

$$[H]\{h_0\} + [S]\left\{\frac{\partial h_0}{\partial t}\right\} + \{G\} = \{F\} \qquad 20]$$

where H [L T^{-1}] is the conductance or stiffness matrix, S [L] is the fluid mass matrix, G [L^2 T^{-1}] is the body force vector and F [L^2 T^{-1}] is the boundary flux vector. All matrices and vectors are defined in detail by Frind (1982). G represents density effects and is, therefore, of special interest in this study. The global body force vector G can be written as sum of all elemental vectors G^e.

$$G = \sum_e G^e \qquad [21]$$

It follows from Equations 18 to 20 that the entries G_i^e [L^2 T^{-1}] of the vector G^e can be calculated following

$$G_i^e = \iint_{A^e} \left(K_0^{fr} \gamma \bar{c} \frac{\partial w_i}{\partial z} \right) dx\, dz \qquad i = 1,2,3,4 \qquad [22]$$

where $\bar{c}$ [--] is the average solute concentration in element e. For a vertical fracture element, Frind (1982) integrates in Equation 22 and obtains the solution as

$$G^e = K_0^{fr} \gamma \bar{c} \frac{L_x}{2} \begin{Bmatrix} -1 \\ -1 \\ 1 \\ 1 \end{Bmatrix} \qquad [23]$$

where the vector entries on the right-hand side refer to the four nodes of a two-dimensional vertical element. For an inclined element, however, the approximation function w_i will vary in space and, therefore, integrating in Equation 22 becomes a surface integral calculus problem.

Following Thomas and Finney (1988), the integral of a function f(x,y,z) over a surface S in space, described by the function F(x,y,z) = constant (Figure 3), can be calculated by evaluating a double integral over the projection or shadow of S on a coordinate plane in the form

$$\iint_R f(x,y,z)\, dR = \iint_R f(x,y,z) \frac{|\nabla F|}{|\nabla F \cdot p|} dA \qquad [24]$$

where R is the shadow region on the ground plane beneath the surface S and p is a vector normal to R. The projection of S in the xz-plane is considered in order to obtain the same perspective as in Frind (1982). In this case, the inclined element becomes pseudo-vertical. From Figure 2, equation F(x,y,z) = constant of the surface S, defining the plane of the fracture face, can be derived as $L_z\, y - L_y\, z = 0$ and we have

$$S : F(x,y,z) = L_z\, y - L_y\, z \qquad [25]$$

$$|\nabla F| = \sqrt{L_y^2 + L_z^2} \qquad [26]$$

$$|\nabla F \cdot p| = L_z \qquad [27]$$

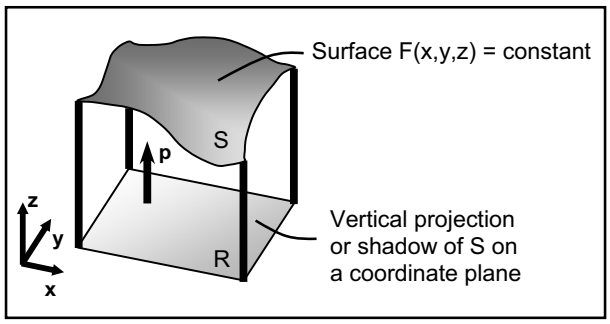

Figure 3. Projection of S on a coordinate plane (Thomas and Finney, 1988).

Using Equations 25, 26 and 27, Equation 24 becomes

$$\iint_R f(x,y,z)\, dR = \iint_R f(x,y,z) \frac{\sqrt{L_y^2 + L_z^2}}{L_z} dx\, dz \qquad [28]$$

where dA = dx·dz. With the function

$$f(x,y,z) = K_0^{fr} \gamma \bar{c} \frac{\partial w_i}{\partial z} \qquad [29]$$

which must be integrated. The entries of the elemental body force vector are given by

$$G_i^e = \int_0^{L_z} \int_0^{L_x} \left(K_0^{fr} \gamma \bar{c} \frac{\partial w_i}{\partial z} \right) dx\, dz \qquad i = 1,2,3,4 \qquad [30]$$

where K_0^{fr} is constant but with an orientation that does not coincide with the global z-direction. Therefore, the above integral has to be evaluated in the local coordinates $\bar{x},\bar{y},\bar{z}$. The required transformation is a rotation around the x-axis by angle φ and can be written in matrix form as

$$\begin{bmatrix} 1 & 0 & 0 \\ 0 & \cos\varphi & -\sin\varphi \\ 0 & \sin\varphi & \cos\varphi \end{bmatrix} \cdot \begin{Bmatrix} x \\ y \\ z \end{Bmatrix} = \begin{Bmatrix} \bar{x} \\ \bar{y} \\ \bar{z} \end{Bmatrix} \quad [31]$$

Thus, we have the relationships

$$\bar{y} = y \cdot \cos\varphi - z \cdot \sin\varphi \quad [32]$$

$$\bar{z} = y \cdot \sin\varphi + z \cdot \cos\varphi \quad [33]$$

$$z = -\bar{y} \cdot \sin\varphi + \bar{z} \cdot \cos\varphi \quad [34]$$

which yields the following derivatives

$$\frac{\partial \bar{z}}{\partial z} = \cos\varphi \quad [35]$$

$$\frac{\partial z}{\partial \bar{z}} = \cos\varphi \quad [36]$$

that will be used below. The integral of Equation 30 is rewritten in terms of local coordinates by first substituting the derivative by means of the chain rule

$$\frac{\partial w_1}{\partial z} = \frac{\partial w_1}{\partial \bar{z}} \cdot \frac{\partial \bar{z}}{\partial z} \quad [37]$$

and, second, by replacing the elementary volume by

$$dx\,dz = \det J \cdot d\bar{x}\,d\bar{z} \quad [38]$$

The Jacobian matrix J [--] collapses to the simple 1 x 1 matrix

$$J = \left[\frac{\partial z}{\partial \bar{z}} \right] \quad [39]$$

whose determinant is given by Equation 36. Expressing a linear approximation function for node 1 in local coordinates gives its spatial derivative as

$$\frac{\partial w_1}{\partial \bar{z}} = \frac{\bar{x} - L_x}{L_x H} \quad [40]$$

with the hypotenuse $H = \sqrt{L_y^2 + L_z^2}$. Now use can be made of Equations 35 to 39 to rewrite Equation 30 as

$$G_1^e = \int_0^{H} \int_0^{L_x} \left(K_0^{fr} \gamma \bar{c} \frac{\bar{x} - L_x}{L_x H} \cos^2\varphi \sqrt{1 + \frac{L_y^2}{L_z^2}} \right) d\bar{x}\,d\bar{z} \quad [41]$$

Repeating steps 40 and 41 for nodes 2, 3 and 4 with a final integration in Equation 41 yields the elemental body force vector G^e for arbitrarily inclined fracture faces in the form

$$G^e = K_0^{fr} \gamma \bar{c} \frac{L_x}{2} \cos\varphi \begin{Bmatrix} -1 \\ -1 \\ 1 \\ 1 \end{Bmatrix} \quad [42]$$

3. MODEL VERIFICATION

The model has been verified by reproducing known solutions for variable-density transport in porous media. Although not shown here, both the Elder (1967) 2D experiment as well as the 3D experimental results presented by Johannsen et al. (2002), with the parameters given in Oswald and Kinzelbach (2004), could be very well reproduced.

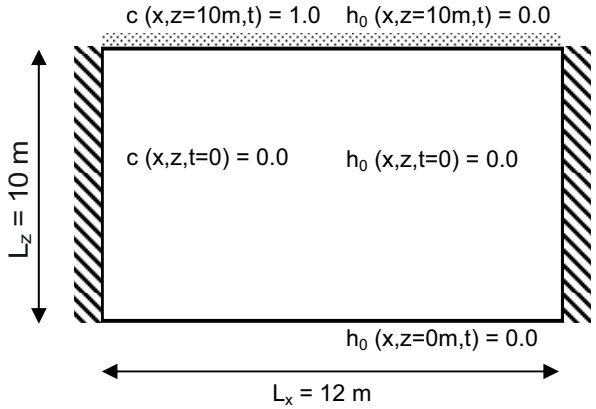

Figure 4. Domain geometry, boundary/initial conditions.

Variable-density transport in vertical fractures was verified by reproducing results presented by Shikaze et al. (1998). For the case of an inclined fracture (φ=45°), the code was verified by comparing the results from two different scenarios run with HydroSphere, for the domain shown in Figure 4. A 3D mesh is used to discretize the domain of unit thickness, $\Delta x=\Delta z$=0.1 m and Δy=1.0 m. The mesh contains 12,221 nodes and 12,000 3D block elements. The left and right boundaries are impermeable whereas the top and bottom are first-type boundaries where the equivalent freshwater head is equal to zero. Similar to Shikaze et. al (1998), the top of the domain is assumed to be a salt lake with a constant concentration equal to 1.0. All other boundaries are assigned zero dispersive flux for transport. In scenario 1, an inclined fracture was discretized only with 2D inclined faces running across the 3D block elements forming the mesh. In a second scenario, the inclined fracture consisted of only vertical

and horizontal faces (Figure 5) corresponding to faces of the 3D block elements.

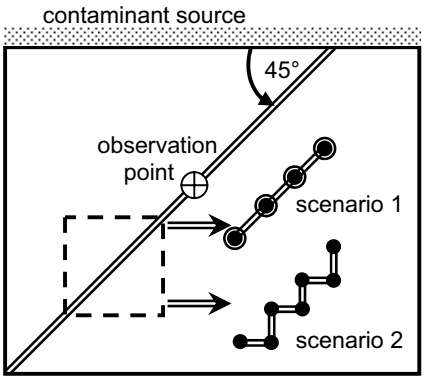

Figure 5. Different discretizations of an inclined fracture.

To account for the longer path along the fracture of scenario 2, the fracture velocities in this scenario were multiplied at each time step by a correction factor. The breakthrough curve was simulated at the observation point as shown in Figure 5 using the model parameters from Table 1. Figure 6 reveals that the two results match. In addition, mass fluxes, mass balance as well as maximum fracture and matrix velocities of the two scenarios were successfully compared (results not shown). Therefore, the code was found to be adequately verified with respect to density effects in inclined fractures.

Table 1. Model parameters used

Parameter	Value
Freshwater density (ρ_0)	1000 kg m^{-3}
Maximum water density (ρ_{max})	1200 kg m^{-3}
Fluid dynamic viscosity (μ)	$3.545 \cdot 10^{4}$ kg m^{-1} a^{-1}
Fluid compressibility (α_{fl})	$4.42 \cdot 10^{-25}$ kg^{-1} m a^2
Acceleration due to gravity (g)	$9.75 \cdot 10^{15}$ m a^{-2}
Factor of tortuosity (τ)	0.1
Matrix compressibility (α_m)	$2.51 \cdot 10^{-24}$ kg^{-1} m a^2
Matrix permeability (κ_{ij})	10^{-15} m^2
Matrix porosity (ϕ)	0.35
Matrix longitudinal dispersivity (α_l)	0.1 m
Matrix transverse dispersivity (α_t)	0.005 m
Fracture long. dispersivity (α_l^{fr})	0.1 m
Fracture transv. dispersivity (α_t^{fr})	0.1 m
Fracture aperture (2b)	150…250 μm
Free-solution diffusion coeff. (D_d)	0.15768 m^2 a^{-1}

4. ILLUSTRATIVE EXAMPLE

With HydroSphere's 2D random fracture generator, irregular fracture networks have been produced to investigate the development of a dense plume for the system shown in Figure 4. The model accounts for spatiotemporal density variations, advection, dispersion and diffusion in both the porous matrix as well as in the fractures.

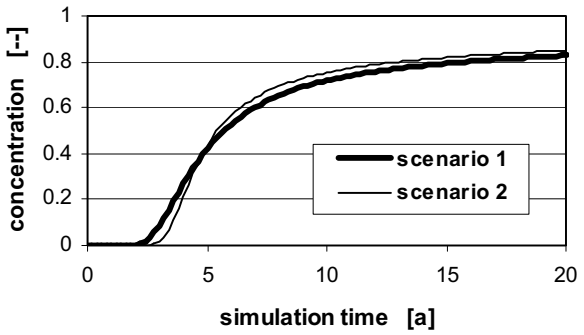

Figure 6. Breakthrough curve at an observation point.

4.1 Generating the Fracture Network

To generate the fracture network, it is assumed that fracture traces are distributed lognormally (Mathab et al., 1995) and that fracture apertures obey an exponential distribution. The aperture is assumed to be constant for a single fracture. Furthermore, the fractures are assumed to of tectonic origin, leading to a conjugated system of two fracture families (Figure 7). Therefore, fracture orientations (φ) follow a two-peak Gaussian distribution with the peaks at -30° and +30°.

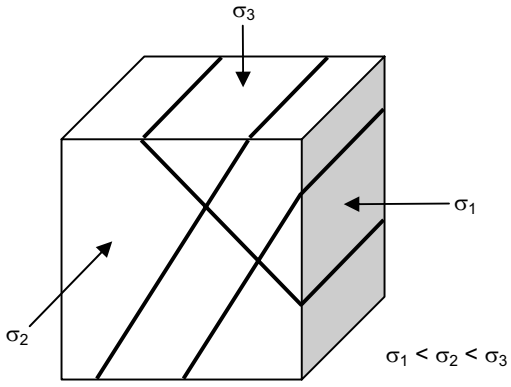

Figure 7. Conjugated system of two fracture families.

4.2 Variable-Density Transport in a Complex Fracture Network

A set of 25 random fracture networks has been generated. In each of these networks, the apertures are distributed exponentially between 150 and 250 μm. For the system shown in Figure 4, with parameters from Table 1, several transient simulations with constant time step size of 1 month were run. The output was observed at 2 years simulation time. For statistically equivalent systems, completely different behavior is observed depending on the spatial location of fractures representing high-permeability zones. Results range from virtually stable in Figure 8a to entirely erratic and unstable in Figure 8c. The formation of instabilities is restricted to the highly permeable fracture zones. Thus, the fracture network

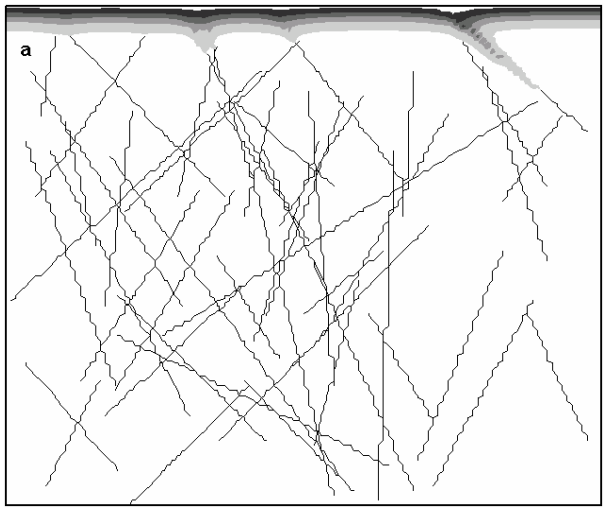

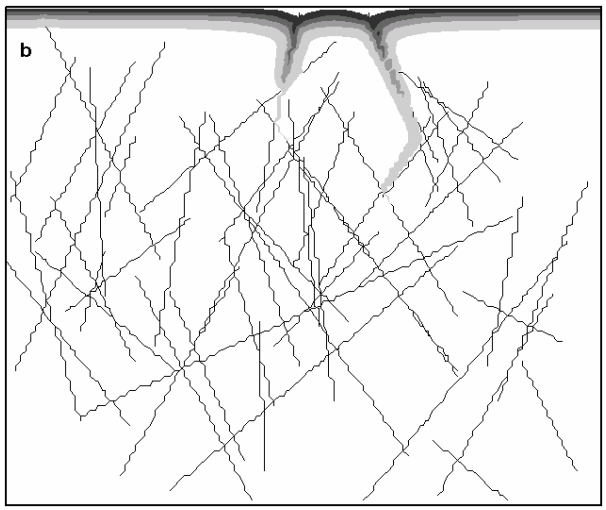

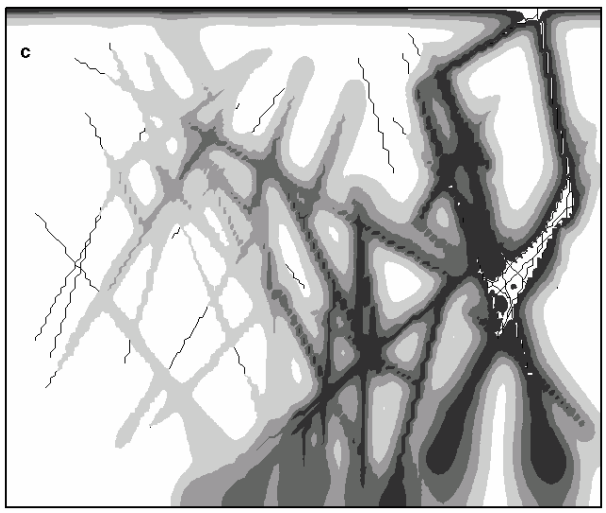

Figure 8. Simulated concentration at 2 years for 3 different fracture networks. Darker colors correspond to high concentration and lighter colors to low concentration.

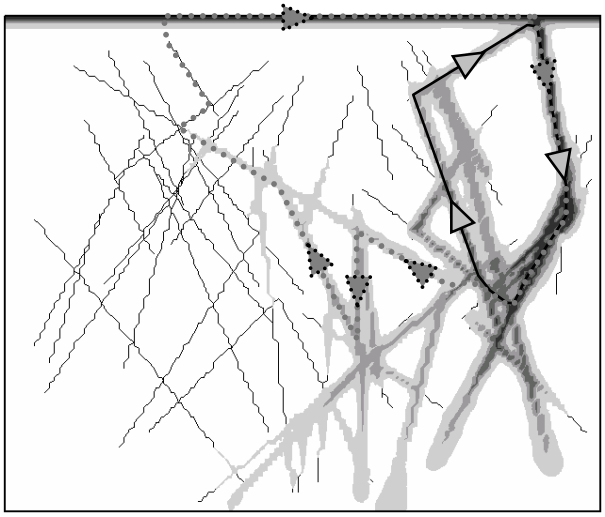

Figure 9. Result of the simulation for the network shown in Figure 8c at 0.5 years, with two convection cells highlighted.

dictates the value of the perturbation wavelength λ, which is the ratio between the domain length (here 12 m) and the number of fingers. The number of fingers in the three cases is 4, 2 and 1, respectively, leading to wavelengths of 3 m, 6 m, and 12 m, respectively. Clearly, shorter wavelengths are more stable, whereas systems with long wavelengths are unstable. This observation corresponds to the findings of Simmons et al. (2001) who examined variable-density transport in statistically equivalent heterogeneous porous media.

However, as opposed to density-driven transport in porous media, the number of instabilities in fractured media does not change with time. Simmons et al. (1999) demonstrated that in a sandy aquifer, the number of fingers decreases with time because large fingers increase, which, in turn, decreases the number of small fingers. In fractured media, however, this is not the case because the location of the fingers is strongly controlled by the geometry of the fracture network.

Furthermore, plume development in fractured media is influenced by the formation of convection cells. Figure 9 shows two selected streamlines of the velocity field. The flow direction in the dominant fracture at the top right corner is downward and upward in other fractures. Figure 9 also shows that only one instability develops, with a corresponding perturbation wavelength of 12 m, because the two fractures close to the surface that seem to be contaminated by the source, located on top of the system, are actually contaminated from below.

4.3 Sensitivity Analysis for the Complex Fracture Network Problem

The model is applied to assess the impact of parameter uncertainties on the plume transport. Eight sets of simulation trials were carried out where single physicochemical properties were modified as shown in Table 2. The fracture network chosen is similar to the one

depicted in Figure 8a. This allows the behavior of the network as a whole to be examined, not only the behavior of the few fractures that dominate the system as shown in Figure 8c.

Table 2. Parameters used for the sensitivity analysis

Parameter	Low value	High value
Matrix permeability (κ_{ij})	$5 \cdot 10^{-16}$ m^2	$2 \cdot 10^{-15}$ m^2
Matrix porosity (ϕ)	0.25	0.45
Fracture aperture (2b)	50…150 μm	250…350 μm
Free-solution diffusion coefficient (D_d)	0.015768 m^2 a^{-1}	1.5768 m^2 a^{-1}

The simulations indicate that increased matrix permeability destabilized the system because of higher computed Darcy fluxes in the matrix (Equation 5) where

$$K_{ij}^0 = \frac{\kappa_{ij} \rho_0 g}{\mu} \qquad i,j = 1,2,3 \qquad [43]$$

Interestingly, modifying the matrix porosity did not have a significant impact on tracer diffusion from the fractures into the matrix. This is in disagreement with simulation results where the fluid density does not vary. In this case, higher matrix porosity would lead to more matrix diffusion. However, it was observed here that the matrix porosity does have an impact on the velocity field according to

$$v_i = -\frac{K_{ij}^0}{\phi}\left(\frac{\partial h_0}{\partial x_j} + \gamma c n_j\right) \qquad i,j = 1,2,3 \qquad [44]$$

Thus, a low matrix porosity ϕ leads to larger matrix velocities v_i that destabilize the system.
According to the Cubic Law

$$Q^{fr} \sim (2b)^3 \qquad [45]$$

the discharge Q^{fr} in fractures changes with the cube of the fracture aperture 2b. Therefore, uncertainties in aperture size have a major impact on the result, with large apertures promoting instability.
Finally, a high diffusion coefficient leads to a high matrix diffusion and, therefore, to a drop of concentration within the fractures. Hence, due to the loss of tracer into the matrix, the fractures are depleted in solutes resulting in less efficient buoyancy within the fractures. Conversely, low diffusion leads to less matrix diffusion and, thus, the concentration gradients as well as the concentrations in the fractures remain large, resulting in high diffusive as well as buoyancy-driven transport within the fractures.

5. CONCLUSION

The migration of a dense plume in a fracture network lacking a regular pattern is highly sensitive to the network used. The formation of instable fingers is limited to fracture locations. For large perturbation wavelengths, efficient convection cells form in the fracture network, transporting the solutes downward into the aquifer. A sensitivity analysis revealed that the system tends to be unstable for large matrix permeability, low matrix porosity, large fracture apertures and low molecular diffusion.

ACHNOWLEDGEMENTS

We thank the Canadian Water Network (CWN) and the Natural Sciences and Engineering Research Council of Canada (NSERC) for financial support. Author TG thanks the International Council for Canadian Studies (ICCS) and the German Academic Exchange Service (DAAD) for providing a Postgraduate Scholarship stipend.

REFERENCES

AECL (Atomic Energy of Canada Limited), 1994. The disposal of Canada's fuel waste: site screening and site evaluation technology. Pinawa, MN, Canada: Whiteshell Laboratories, 255 pp.

Bear J, 1988. Dynamics of fluids in porous media. New York, NY, USA: Elsevier; 764 pp.

Elder JW, 1967. Transient convection in a porous medium. Journal of Fluid Mechanics, Vol. 27, pp. 609-623.

Frind EO, 1982. Simulation of long-term transient density-dependent transport in groundwater. Advances in Water Resources, Vol. 5, pp. 73-88.

Johannsen K, Kinzelbach W, Oswald SE and Wittum G, 2002. The saltpool benchmark problem – numerical simulation of saltwater upcoming in a porous medium. Advances in Water Resources, Vol. 25, pp. 335-348.

Mathab A, Xu S, Grasso P and Kendorski FS, 1995. Use of alternative distributions for characterizing joint extent and spacing. In: Fractured and Jointed Rock Masses; Myer, Cook, Goodman and Tsang (eds), pp. 199-204.

Oswald SE and Kinzelbach W, 2004. Three-dimensional physical benchmark experiments to test variable-density flow model. Journal of Hydrology, Vol. 290, pp. 22-42.

Shikaze GS, Sudicky EA and Schwartz FW, 1998. Density-dependent solute transport in discretely-fractured geologic media: is prediction possible? Journal of Contaminant Hydrology, Vol. 34, pp. 273-291.

Simmons CT, Fenstemaker TR and Sharp Jr. JM, 2001. Variable-density groundwater flow and solute transport in heterogeneous porous media: approaches, resolutions and future challenges. Journal of Contaminant Hydrology, Vol. 52, pp. 245-275.

Simmons CT, Narayan KA and Wooding RA, 1999. On a test case for density-dependent groundwater flow and solute transport models: The salt lake problem. Water Resources Research, Vol 35, pp. 3607-3620.

Therrien R and Sudicky EA, 1996. Three-dimensional analysis of variably saturated flow and solute transport in discretely-fractured porous media. Journal of Contaminant Hydrology, Vol. 23, pp. 1-44.

Thomas GB Jr. and Finney RL, 1988. Calculus and analytic geometry, 7th edition. Reading, MA, USA: Addison-Wesley Publishing Company; 1136 pp.